https://doi.org/10.5194/nhess-2021-387
Preprint. Discussion started: 17 March 2022

Natural Hazards and Earth System Sciences
Discussions

Modelling tides and storm surge using intertidal bathymetry derived from the waterline method applied to multispectral satellite images

Wagner L.L. Costa[1], Karin R. Bryan[1], Giovanni Coco[2]

[1]School of Science, University of Waikato, 124 Hillcrest road, E-F link, Hamilton, New Zealand.
[2]School of Environment, University of Auckland, Auckland, New Zealand.

Correspondence to: Wagner L.L. Costa (wc119@students.waikato.ac.nz)

Abstract. Bathymetric data are essential for accurate predictions of flooding in estuaries, because water depth is a fundamental component in the shallow-water hydrodynamic equations used in numerical models. Where LiDAR or acoustic in-situ surveys are unavailable, recent efforts have centred on the use of satellite images to estimate bathymetry (SDB). This work is aimed at (1) determining the accuracy of SDB, and (2) assessing the suitability of the SDB for surge/tidal modelling of estuaries. The SDB is created by extracting the waterline as it tracks over the bathymetry with changing tides, and is applied to 4 different estuaries in New Zealand: Whitianga, Maketū, Ōhiwa and Tauranga Harbour. Results show that the waterline method provides similar bathymetries to the LiDAR with root-mean squared error equal to 0.2 m, and it is slightly improved when two proposed correction methods are applied to the bathymetry derivations: the removing of statistical bias (by 2cm) and hydrodynamic modelling correction (by 1 cm). Finally, the use of SDB in numerical simulations of surge levels is assessed for Tauranga Harbour with 4 different scenarios that explore the use of SDB in comparison to bathymetry data collected using non-satellite survey methods. One of these includes the well-known Stumpf-ratio method to extract the SDB of subtidal regions (so that only satellite information is used). The use of the satellite derived bathymetry in hydrodynamic models does not result in significant differences in terms of water levels, when compared with the scenario modelled using surveyed bathymetry.

1 Introduction

Coastal flooding events have become increasingly concerning because of growing storm intensity (Emanuel, 2005; Sobel et al., 2016; Webster et al., 2005) and sea-level rise, which will potentially increase the risk exposure of coastal communities (Nicholls and Cazenave, 2010; Oppenheimer et al., 2019). In practice, predicting flooding events depends on understanding the contribution from the astronomical tide, wave run-up, fluvial discharge, vertical land motion, and changes in the sea-level. In coastal zones, these processes can interfere in each other such as in, for instance, the tide-surge interactions (Spicer et al., 2019; Wankang et al., 2019; Zheng et al., 2020). In the specific case of estuaries, bathymetric data are essential for predictions (Cea and French, 2012; Parodi et al., 2020; Pedrozo-Acuña et al., 2012) because water depth is a fundamental component in the shallow-water hydrodynamic equations used in surge modelling. Water depth controls the amplitude and phase (timing) of the propagating tide as well as the estuary's geometry and length (which can cause shoaling and choking) and bed-shear stress

https://doi.org/10.5194/nhess-2021-387
Preprint. Discussion started: 17 March 2022


Natural Hazards and Earth System Sciences Discussions

(which reduces energy due to its effect on friction). The estuary's bathymetry is also fundamental for studying the tidal response to sea-level rise (Du et al., 2018).

Techniques to measure bathymetry in shallow water have evolved rapidly (Jawak et al., 2015). Acoustic techniques (e.g. echo-sounders) are known to produce highly-accurate data; however, such methods are constrained by cost, inaccessibility of remote areas, and environmental conditions in shallow water and estuaries (e.g. water turbidity, low tide navigational restrictions). To overcome these issues, efforts have centred on using spaceborn remote sensing (RS) techniques (Bishop-Taylor et al., 2019; Bué et al., 2020; Caballero and Stumpf, 2019), and there are several RS techniques to estimate bathymetry, each one of them having its own advantages/disadvantages and accuracy depending on the environment in which they are applied and its depth range (Gao, 2009). In comparison to acoustic techniques, RS methods are faster and applicable to a wider range of environments, including remote and/or shallow coastal waters (Caballero and Stumpf, 2019; Ehses and Rooney, 2015; Lyzenga, 1985), and allow bathymetry to be estimated over extensive areas which would not be accessible using traditional methods (Bishop-Taylor et al., 2019).

For shallow waters, between 0-30m depths, some SDB methods (Caballero and Stumpf, 2019; Stumpf et al., 2003) use a radiometric approach, which uses the property that different wavelengths are attenuated to varying degrees in the water column. In these cases, an empirical formula is used to fit the relationship between the ratio of reflectance of different spectral bands (resolved on a pixel-by-pixel basis) to the measured in-situ water depth. However, limitations include: the requirement of in situ bathymetric data to calibrate the empirical relationships; the decline in performance caused by variation in the benthic substrates and the inherent optical properties (IOPs) such as water turbidity and bottom reflectance, often occurring in enclosed seas, bays and estuaries (Morris et al., 2007). Novel techniques using physically based algorithms such spectral optimization algorithm (SOA) (Lee et al., 2011; Lyzenga et al., 2006; Wei et al., 2020) and methodologies to correct the water turbidity (Caballero and Stumpf, 2020) have been developed to solve the empirical model's limitations. Bué et al., 2020 proposed a technique that generates high density bathymetric data for intertidal zones by using a logistic regression equation to fit reflectance in the near infrared band (NIR) of multispectral images to the observed tide.

Another SDB method that is particularly appropriate for intertidal zones, the waterline method, has been widely applied to Synthetic Aperture radar - SAR (Catalao and Nico, 2017; Huang et al., 2001; Mason and Davenport, 1996) and multispectral (Khan et al., 2019) images. This method functions by detecting the land-water boundary in an image, and associating this line to the tidal height observed at the time of the image acquisition. The tidal height can be predicted by a regional tide model (Bishop-Taylor et al., 2019; Khan et al., 2019) or from a local tide gauge (Mason et al., 1997). The waterlines are mapped over a number of images (each acquired at a different tidal level), and the resulting collection of waterlines is interpolated in the intertidal domain, generating a digital elevation model (DEM). The approach assumes that estuary morphology is constant throughout the period of image acquisition. The main disadvantages of this method are: the low number of estimated waterlines due to a reduction in the number of available images as consequence of cloud coverage; the dependency of accuracy on the number of processed images; the negative influence of bathymetric slope and complexity on waterline coverage; and, in the

https://doi.org/10.5194/nhess-2021-387
Preprint. Discussion started: 17 March 2022

Natural Hazards and Earth System Sciences Discussions

case of SAR images, the sensitivity of the sensors to windy conditions; i.e. changes in the backscatter signal due to the increased rugosity caused by the strong wind blowing in the water surface (Liu et al., 2013; Mason et al., 2001).

As SDB techniques have developed, cloud computation and storage systems such as Google Earth Engine (Gorelick et al., 2017) have advanced considerably, enhancing the capacity to easily manage large geographical datasets, which has allowed global-scale studies in coastal science to evolve rapidly. For instance, databases now exist on the distribution and changes to global tidal flats (Murray et al., 2019) as well as a global estimation of coastline position (Vos et al., 2019). Combining recent SDB methods and innovative cloud data storage and computation, extensive databases of satellite images can be quickly and easily processed, enabling bathymetry for multiple estuaries to be estimated routinely.

Despite the wide and growing application of SDB methods, it is not yet clear whether the accuracy of the resulting bathymetry is suitable for coastal tidal or storm surge modelling, both critical to managing adaptation to sea level rise. Only limited studies exist in related to the use of SDBs in numerical modelling, such as data assimilation in a coastal morphodynamic model (Mason et al., 2010). Our study is aimed at: (1) determining whether satellite imagery can be used to extract accurate intertidal bathymetric data; and, (2) assessing the use of the SDB for hydrodynamic modelling of estuaries.

2 Methods

The method was divided into 2 main steps, Fig. 1: (1) the SDB estimation (using the waterline method and, for Tauranga Harbour only, the Stumpf-ratio method); and (2) the hydrodynamic modelling assessment. In addition, as part of step 1, two methods were trialled to remove a bias highlighted by a comparison to LiDAR observations (symbolised by the red and green fonts in Fig. 2).

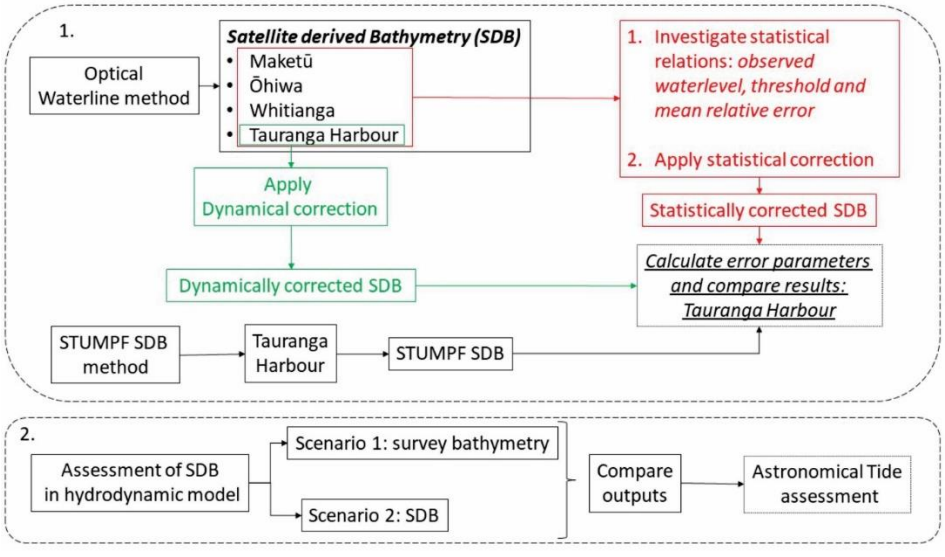

Figure 1: A flow chart showing the steps taken to derive the SDB and test its utility in modelling.

https://doi.org/10.5194/nhess-2021-387
Preprint. Discussion started: 17 March 2022


Natural Hazards and Earth System Sciences Discussions

2.1 Study site and database

The study areas are four estuaries located in the east coast of Aotearoa New Zealand's North Island; three in the Bay of Plenty region: Tauranga, Ōhiwa and Maketū harbours and one in the Coromandel: Whitianga harbour, Fig. 2A. The studied sites have microtidal regimes — the spring tidal range varies between 1.4 m to 1.9 m within estuaries – and all have wide intertidal areas covering from 58% to 84% of the estuaries' total area (Hume et al., 2016). For instance, the extent of the tidal flats is evident in Tauranga Harbour by comparing low (e.g. Fig. 2B) and high (e.g. Fig. 2C) tide images; the intertidal zone is easily distinguished by the colour of sand accentuating reflectance in the near infrared band. Associated with tidal flats, mangrove forest can be observed in all the studied estuaries as well as vast seagrass banks for Maketū, Ōhiwa and Tauranga Harbour (the latter was studied in Ha et al., 2020).

For the implementation of SDB techniques, only tidal levels and imagery are needed. We used additional in situ bathymetric data to validate the SDB. For Bay of Plenty region, the historical tide levels were extracted from the Bay of Plenty Council data portal (https://envdata.boprc.govt.nz/); the bathymetry data consist of the LiDAR survey for which a 1x 1m resolution dataset was available on the Land Information New Zealand data portal (https://data.linz.govt.nz/). For Whitianga, we acquired both water level time series and elevation data (LiDAR) by request through the Thames-Coromandel District Council's website (http://www.tcdc.govt.nz/). The LiDAR data have a vertical accuracy of ± 0.2 m and ± 0.6 m horizontal with 95% of confidence for Bay of Plenty. To calculate the SDB's accuracy, all LiDAR data were converted to the local vertical datum (i.e., Moturiki 1953), which is 0.13 m below mean-sea level (MSL), by using the GEOID elevation grids available in LINZ data portal.

We used European Space Agency (ESA) Copernicus Sentinel satellite images accessed through Google Earth Engine (Gorelick et al., 2017), from spacecraft Sentinel 2A and B, product type level-2A. The Sentinel-2 products are composed of elementary tiles, which are 100x100 km2 ortho-images in UTM/WGS84 projection, with a revisit frequency of 5 days in the Aotearoa New Zealand region. The level-2A product type provides bottom-of-atmosphere (BOA) images, which are corrected for the effects of the top-atmosphere. Each image has the spectral resolution of 12 bands with spatial resolution differing between 10, 20 and 60 m depending on band. Here we used the green (band 3, 560 nm), blue (band 2, 490 nm) and near infrared (band 8, 842 nm) bands, all of them with 10m spatial resolution.

In summary, for each estuary, a complete set of LiDAR, tidal gauge observations and a satellite images was obtained for this study. For example, the Tauranga Harbour dataset is shown in Fig. 2: the location of the tide gauges (Omokoroa, Hairini and Oruamatua) and the intertidal exposure during low tide (Fig. 2B) and high tide (Fig. 2C), as well as their water level record for the acquisition period of the satellite images (Fig. 2D). In the specific case of Tauranga Harbour, where a hydrodynamic model was run, additional bathymetric data was needed to supplement the SDB for the deepest parts of the model domain (e.g. tidal channels and coastal zone). The bathymetry data ("the multi-source bathymetry") used in the hydrodynamic model was assembled using a combination of data from multiple sources: Multibeam survey (Port of Tauranga, 2017), LiDAR (2008 from AAMHATCH and 2016 from LINZ) and LINZ hydrological charts NZ 5411, 2016. These were converted from chart datum (lowest astronomical tide) to mean sea level by adding a uniform value of 1.05m to the data.

https://doi.org/10.5194/nhess-2021-387
Preprint. Discussion started: 17 March 2022

Natural Hazards and Earth System Sciences
Discussions

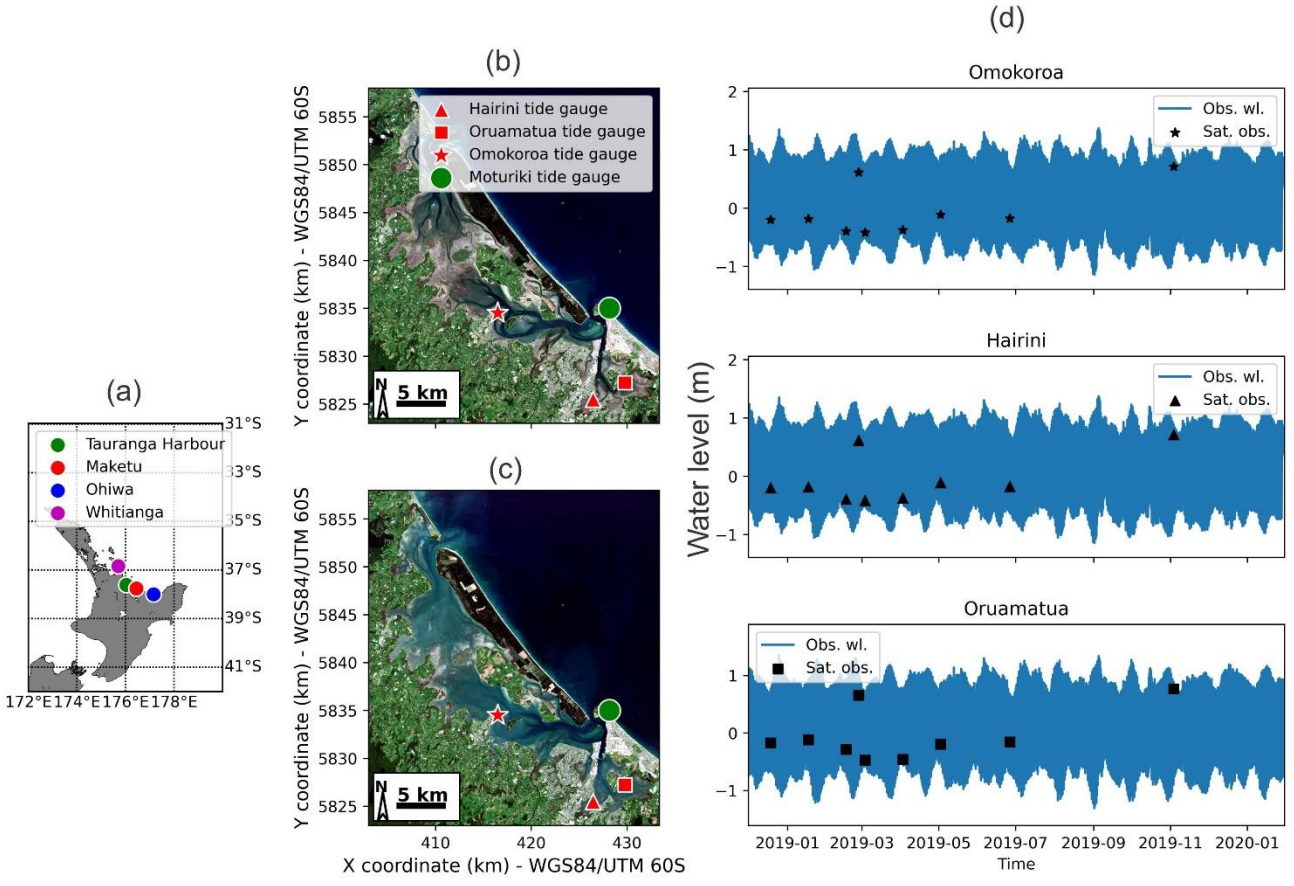

Figure 2: Study sites. The New Zealand estuaries where the SDB method was tested (a). Tauranga Harbour and tide gauge locations during low tide (b) and high tide (c). Water level time series from the local tide gauges during the period over which satellite images were acquired (d). Background image: ESA Sentinel 2A.

2.2 Satellite-derived bathymetry techniques

The process of generating the SDB in intertidal zones using the waterline method was composed of 4 stages. First, image pre-processing was done through the Google Earth Engine application (Gorelick et al., 2017) using the Google Colaboratory environment. In this step, for each estuary, a search was performed in the Copernicus database, for Sentinel 2A and B, product type level-2A, to extract an image collection where each image covers the estuary domain and is cloud-free. The number of images corresponding to each estuary's collection and environmental properties (e.g. coverage of intertidal zone in the estuary; spring tidal range) is shown in Table 1.

https://doi.org/10.5194/nhess-2021-387
Preprint. Discussion started: 17 March 2022


Natural Hazards and Earth System Sciences Discussions

130

Table 1: Number of images in the image collection for each estuary.

Estuary	*Nº of images in the collection*	*Total intertidal area* (Hume et al., 2016)	*Spring tidal range*
Tauranga Harbour	9	77%	1.75 m
Ōhiwa	7	84%	1.9 m
Maketū	15	58%	1.4 m
Whitianga	8	72%	1.7 m

Second, we identify the intertidal zone by calculating the temporal variability at each pixel of the Normalized Difference Water
135 Index (NDWI) over the entire image collection (McFeeters, 1996), using Equation 1:

$$\sigma(x,y) = \sqrt{\frac{1}{n}\sum_{i=1}^{n}(NDWI_i - \overline{NDWI})^2}; \quad (1)$$

$$NDWI = \frac{\rho_{green}-\rho_{nir}}{\rho_{green}+\rho_{nir}};$$

where x and y are the pixel coordinates, n is the number of images in the collection, ρgreen and ρnir are reflectance of the green and near infrared bands of Sentinel-2 images respectively. As a result, one single grey scale image is produced
140 representing the NDWI temporal standard deviation (σ), Fig. 3. Since the NDWI in each pixel in the intertidal zone is expected to vary more because of the constant change between exposed (low tide) and inundated (high tide) conditions, we assume that the highest values of standard deviation will occur in the intertidal zones. To identify the tidal flat areas, we set a threshold by using the Otsu approach (Nobuyuki Otsu, 1979). The Otsu method identifies the optimum threshold between two classes of data in the image distribution that maximizes the value of the within-class variance, defined as a weighted sum of variances of
145 the two classes:

$$\sigma_w^2(t) = \omega_0(t)\sigma_0^2(t) + \omega_1(t)\sigma_1^2(t); \quad (2)$$

where ω_0 and ω_1 are the probabilities of the two classes separated by threshold t, and σ_0^2 and σ_1^2 are the variances of these two classes. The intertidal zone identified for Tauranga Harbour is presented in Figure 3. A polygon is generated in order to mask the tidal flat in every image, avoiding needless image processing outside the intertidal area.

https://doi.org/10.5194/nhess-2021-387
Preprint. Discussion started: 17 March 2022

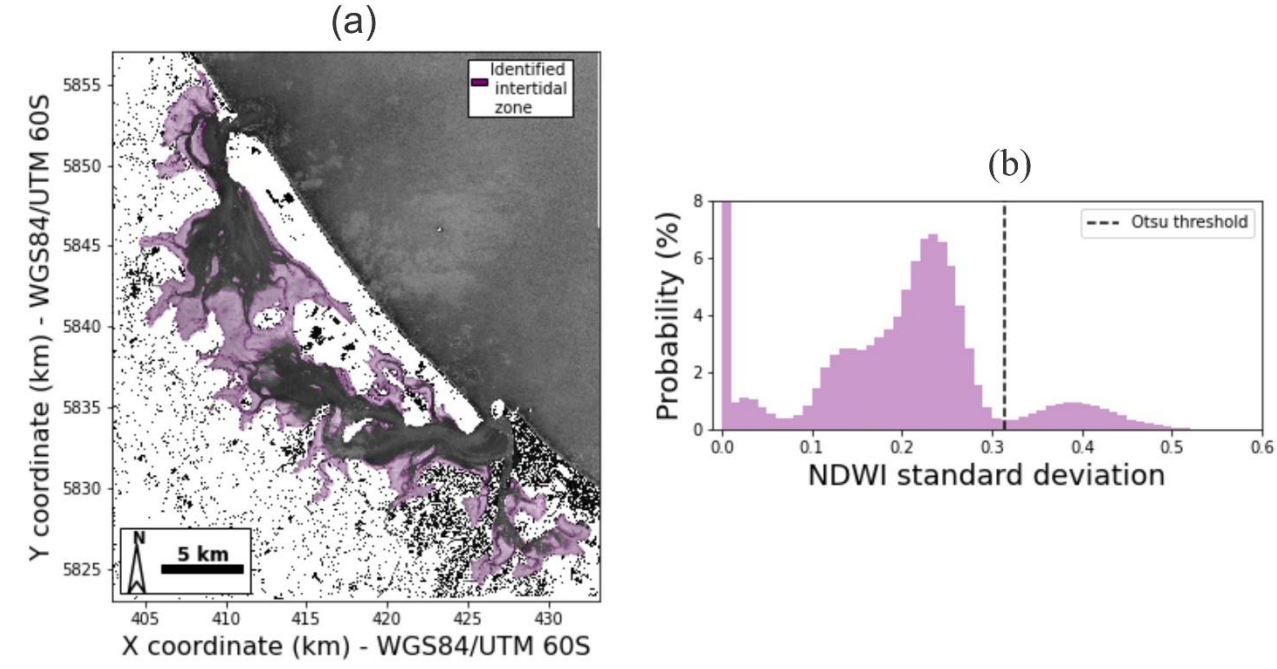

Figure 3: Identified intertidal areas. (a) Intertidal areas identified using the NDWI standard deviation from the Tauranga Harbour image collection. Determination of the Otsu threshold for the identification of the intertidal zone (b).

Third, the position of the waterline in each image is defined by applying the algorithm "Finding_Contours" from the scikit.measure (Van Der Walt et al., 2014) Python library. This contour extraction method searches for a given value (threshold) in a two-dimensional array of pixels, using the 'marching squares' algorithm (Lorensen and Cline, 1987) to identify precise contour boundaries by linearly interpolating between adjacent pixel values. Again the adaptive Otsu threshold is used to find the location of the waterline from the NDWI maps for each image, Fig. 4.

Fourthly, once the waterline for a given image is identified, a height value is assigned to it accordingly to the corresponding tide level observed at the closest tide gauge (Omokoroa for the Tauranga Harbour case study, Fig. 2D).

https://doi.org/10.5194/nhess-2021-387
Preprint. Discussion started: 17 March 2022

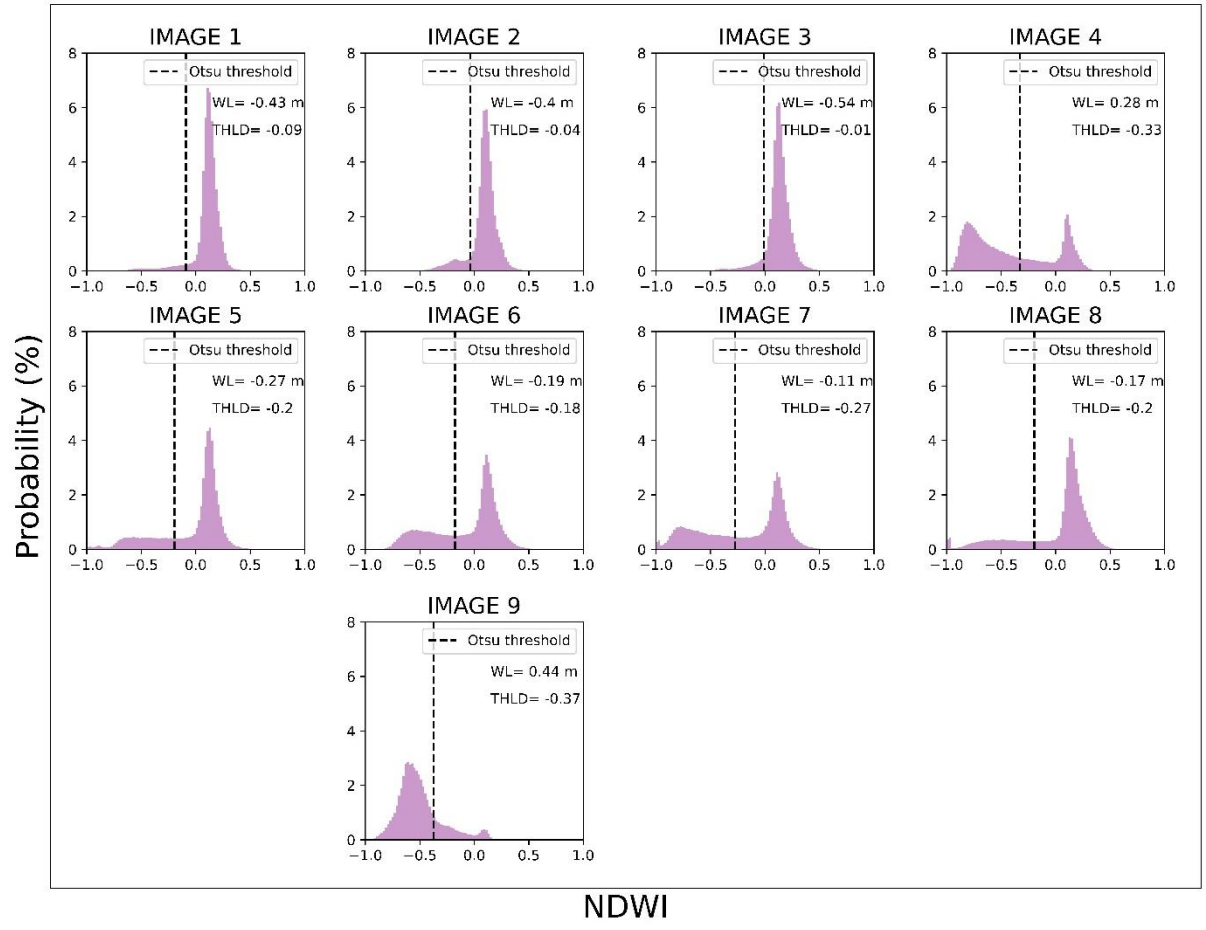

Figure 4: Otsu threshold applied to identify the waterline coordinate points for each image in the Tauranga Harbour image collection. The observed water level from the Omokoroa tide gauge at the moment of the image acquisition is also shown in each panel (marked WL).

Additionally, the Stumpf-ratio method (Stumpf et al., 2003) was applied in Tauranga Harbour for intertidal and deeper areas separately. In the first case it was used to compare with the waterline-SDB; and in the second case, to use in the hydrodynamic modelling —following Costa et al., (in press), where the method was trialled in a sub-estuary of Tauranga Harbour — detailed information about the method and the estimates for tidal flats are provided in Supplement A and Fig. S1.

2.3 Assessment of framework performance

We assessed the accuracy of the SDB and hydrodynamic model performance by calculating the following error metrics: root mean square error (RMSE), maximum absolute error (MAE), relative error (RE), coefficient correlation (R2), and bias (BIAS) (Eq. 3–7 respectively). In the corresponding equations, h_{est} is the estimated value (e.g. SDB, hydrodynamic model output) and h_{obs} is the observed value (e.g. LiDAR data, tide gauge measurements). In the case of SDB evaluation, its relative error can be either negative or positive, when the SDB is shallower or deeper than the LiDAR data, respectively. For illustrating this

https://doi.org/10.5194/nhess-2021-387
Preprint. Discussion started: 17 March 2022

Natural Hazards and Earth System Sciences
Discussions

calculation, a schematic is in Fig. 5, showing that although the error is evaluated in terms of height differences, it can arise because of either horizontal or vertical inaccuracies.

$$RMSE = \sqrt{\sum_{i=1}^{n} \frac{(h_{est} - h_{obs})^2}{n}}; \quad (3)$$

$$MAE = \max_{i=1\ldots n} |h_{est}\mathrm{i} - h_{obs}\mathrm{i}|; \quad (4)$$

$$RE = h_{obs} - h_{est}; \quad (5)$$

$$R^2 = \frac{\sum_{i=1}^{n} (h_{est}i - \overline{h_{obs}})^2}{\sum_{i=1}^{n} (h_{obs_i} - h_{est_i})^2 + (h_{est_i} - \overline{h_{obs}})^2}; \quad (6)$$

$$BIAS = \overline{h_{est}} - \overline{h_{obs}} \quad ; \quad (7)$$

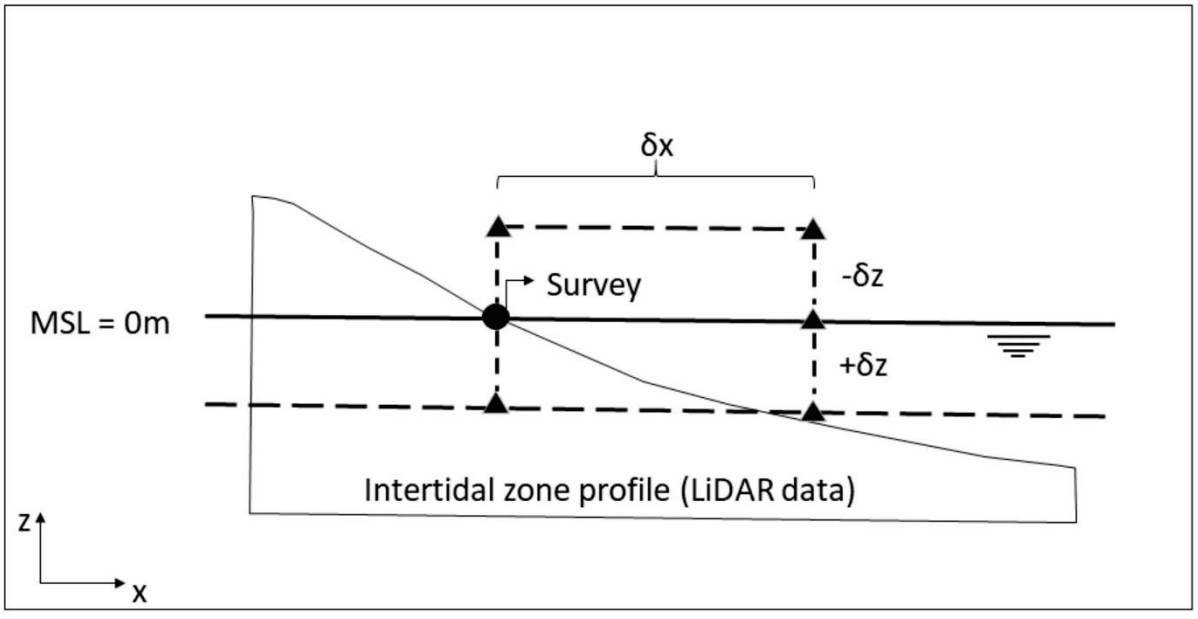

Figure 5: Schematic showing the error calculation where the circle shows the actual location of the water line, and triangles show the location of the remotely sensed shoreline. There are two ways that an error can be caused. The waterline can be detected landward or seaward of its actual location (δx), or the waterline is assigned an elevation that is too high or too low (δz).

2.4 The SDB correction approaches

The accuracy of the waterline SDB method can be limited either by environmental conditions that affect the ability to correctly identify the shoreline — e.g. complexity of the intertidal zone's morphology, presence of seagrass, groundwater seepage leaving a film of moisture on the exposed intertidal (Huisman et al., 2011) — and spatial changes to the tide level, caused by the propagation of the tide through the Harbour. These effects meant that consistent bias in the elevation of the SDB relative to LiDAR were detected. Two different correction methods were tested to improve the SDB: the statistical and the dynamical correction.

https://doi.org/10.5194/nhess-2021-387
Preprint. Discussion started: 17 March 2022


Natural Hazards and Earth System Sciences Discussions

The statistical correction is based on the dependence of the bias on the value of the Otsu threshold (THLD) during each image acquisition, in all the studied estuaries. This correction was developed on the basis that the detected waterline is further seaward or landward of the actual waterline. The dynamical correction assumes that the bias was generated because the water level is higher or lower than the actual waterline, and was developed using a hydrodynamic model to simulate the astronomical tide propagation through the Tauranga Harbour. The model used was the DELFT3D FLOW, and the domain and bathymetry are shown in Fig. S3 (Supplement B), covering the centre to southern part of the Harbour with a 20x20 m resolution grid. The open boundaries were set as free Neuman boundaries in the north and south and the astronomical components were used to force the water level along the seaward boundary. For the latter, harmonic astronomical tidal analysis was undertaken on the Moturiki Island tide gauge using U_tide (Codiga, 2011).

The model was validated to ensure the bed roughness parameters were appropriate by simulating an equinoctial tidal period, from 01/03/2019 to 31/03/2019. The vertical datum in the simulation was the mean-sea level (MSL), the time step used was 0.5 min; the advection scheme for calculating the flooded and dried cells is cyclic, using the water level averaged on the grid cells. The model performance was assessed against tide gauge observations points (Omokoroa, Hairini and Oruamatua) using the RMSE, MAE and R2 (see Sec. 2.3 for explanations). The model shows good approximation to the predicted data, with RMSE varying between 6 and 8 cm, and maximum error (MAE) within 21–26 cm and a correlation (R2) of 0.98 at the three observation points, Fig. S4 (Supplement B).

Ideally, to be able to use the SDB methods for sites where there is no LiDAR coverage, we need a dynamical correction that only uses the SDB to assess the propagation of the tidal wave. After validating the bed roughness, the intertidal bathymetry in the model was replaced by the SDB — which was previously converted from local datum (Moturiki 1953) to MSL by adding 13 cm to its value — using the Delft3D- QUICKIN tool. Using this new depth file, simulations were done for the time period during which each of the 9 images in the image set were acquired. Each case had a simulation period corresponding to the ten-day period prior to the date and time of acquisition of the satellite image. Finally, each point along the satellite-detected waterline was assigned a height value by interpolating the water level model output for the time that correspond to the moment the images were acquired by the satellite.

2.5 Assessing water level simulations with SDB

To evaluate the accuracy of hydrodynamic simulations using SDB against the use of surveyed bathymetry data, we developed 4 different simulation scenarios (Table 2). The S1 is the validated model specified in Sect. 2.4, that uses the multi-source survey bathymetry (i.e. LiDAR, multibeam, digitalised nautical charts) throughout the model domain; this base case represents the “usual” situation when the modeller depends only on the in situ measured bathymetry. In the S2 and S3 scenarios, we replaced the intertidal zone bathymetry with the waterline and Stumpf-derived SDB, respectively, to evaluate which technique would be the best replacement for multi-source data in the tidal flat area. The S4 scenario was developed to assess the use of wholly-SDB derived bathymetry in the entire model domain. For that, the waterline-derived SDB is used in the tidal flat and the Stumpf-derived SDB is used in the deeper areas inside the harbour. To assess the simulations we compared the water level

https://doi.org/10.5194/nhess-2021-387
Preprint. Discussion started: 17 March 2022


Natural Hazards and Earth System Sciences Discussions

225 prediction at the three observation points (Omokoroa, Hairini, and Oruamatua) and the water level output maps in each simulated scenario in terms of RMSE, MAE, and R2.

Table 2: Simulation scenarios to assess the use of SDB in hydrodynamic modelling.

Scenarios	Source intertidal zone	Source deeper areas
S1	surveyed bathymetry	surveyed bathymetry
S2	waterline-derived SDB	surveyed bathymetry
S3	Stumpf-derived SDB	surveyed bathymetry
S4	waterline-derived SDB	Stumpf-derived SDB

230 **3 Results**

3.1 The waterline satellite derived bathymetry

The waterline SDB accuracy, compared to the LiDAR data, for all the studied estuaries is shown in Table 3; the average error was 0.28 m and 1.58 m across all estuaries, for RMSE and MAE respectively. The technique's worst performance was in Ōhiwa estuary (RMSE =0.35 m and MAE= 2 m), Fig. S5, probably due to its complex morphology (i.e. wide intertidal zones,
235 complex narrow channels and irregular bathymetry). Whitianga estuary, Fig. S6, had a similarly higher error for the same reasons. In addition, the length and elongated geometry of Whitianga estuary — 8 km from the mouth to the inner part where the intertidal zone was detected — can amplify errors related to tide wave propagation. Despite their different dimensions, Tauranga Harbour and Maketū (the latter in Fig. S7) have similar performance, probably due to similar water optical properties (i.e. water colour, bed colour, infrared and green bands) and similar bathymetric slopes.

240 **Table 3: Waterline-derived SDB errors for every studied estuary.**

Estuary	*RMSE*	*MAE*	*R2*
Ōhiwa	0.35	2.00	0.90
Whitianga	0.35	1.00	0.97
Maketū	0.22	1.75	0.93
Tauranga Harbour	0.20	1.60	0.86
Average	0.28	1.58	0.91

https://doi.org/10.5194/nhess-2021-387
Preprint. Discussion started: 17 March 2022

Natural Hazards and Earth System Sciences
Discussions

Although the SDB accuracy differs depending on the estuary, the mean relative error (MRE) is strongly linearly-correlated with the observed water level (Z) and the Otsu adaptive threshold (THLD), as shown in Fig. 6. The THLD and Z correlation (R2 = 0.77), Fig. 6 (a), indicates that the Otsu threshold explains approximately 80% of the Z variance in overall. As consequence, THLD and MRE are strongly related (R2 = 0.70) as well as the MRE and Z (R2 = 0.74), Fig. 6 (b) and (c), respectively. Also, we observed a pattern between the MRE and the tide: the MRE increases at high and low tide for all estuaries, and the lowest errors occur during mid-tide. The difference between flooding and ebbing tides do not seem to interfere in the waterline-derived SDB accuracy; we hypothesised that water draining off the intertidal during ebbing tides might cause inaccuracies in waterline detection. The linear trend of the relationship between MRE, Z, tidal level and the Otsu threshold across different estuaries reflects the similarities of these sites in terms of environmental characteristics such as intertidal zone sediment colour, water turbidity/colour, spring tidal range and the coverage of the intertidal area relative to the overall area of the estuary. In Sect. 3.3, we use the relationship between THLD and MRE to remove the bias in the waterline-derived SDB for Tauranga Harbour, what we hereafter called “the statistical correction”.

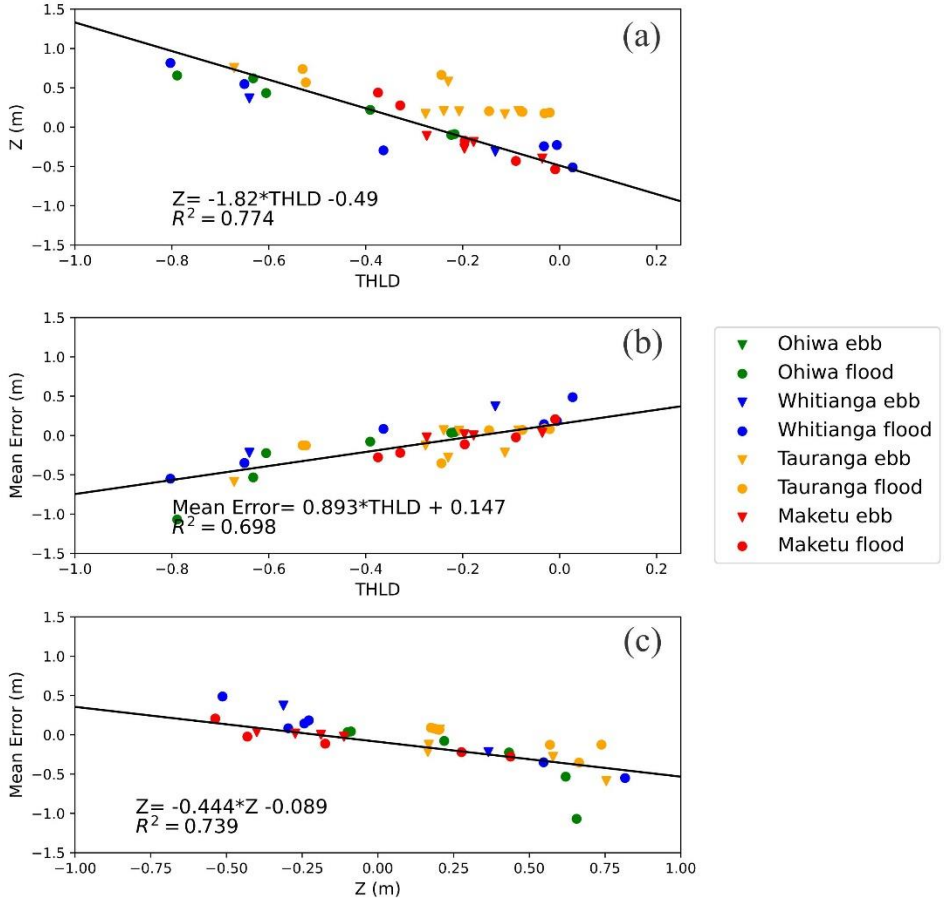

Figure 6: Statistical relationships at all estuaries (Ōhiwa, Whitianga, Tauranga, Maketū): (a) water level Otsu threshold (THLD) and observed water level (Z); (b) THLD and the SDB mean relative error per image; (c) Z and the SDB mean relative error per image R2.

https://doi.org/10.5194/nhess-2021-387
Preprint. Discussion started: 17 March 2022

Natural Hazards and Earth System Sciences
Discussions

3.2 Comparison between the Waterline and Stumpf-ratio methods for intertidal zones

The distribution of the relative vertical error (RE) of Tauranga Harbour's waterline-derived SDB (primary SDB) and Stumpf-derived SDB for intertidal zones are showed in Fig. 7. In the waterline-derived SDB (Fig. 7 (a1), (b1), (c1), and (d1)), gaps between the waterlines occur because of the limited number of images used to cover the entire tidal range; although Sentinel-2 acquires images every 5 days, they are often not useable due to cloud cover. The SDB is generally shallower or further seaward than the LiDAR — as the negative RE indicates (see Sect. 2.3) — with the worst estimates in the tidal flat's upper region (bluer colour dots). The positive RE values are concentrated in the estuary's wide flat region (Fig. 7 (b1)), which has a complex bathymetry. In addition, the extensive banks of seagrass located in this area may also contribute to poor waterline extraction (Fig. 7 (a) and (b)), because seagrass changes pixel reflectance around the waterline.

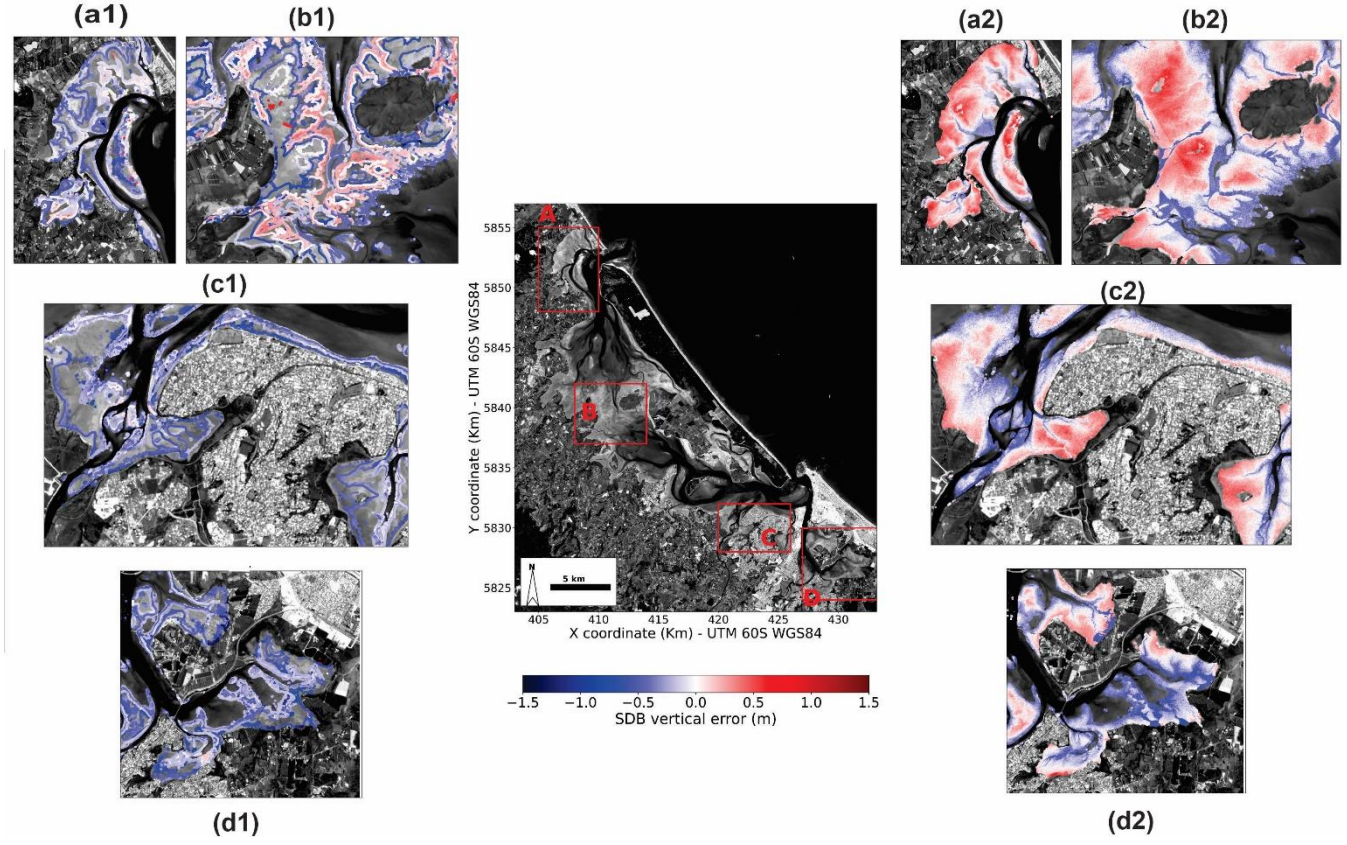

Figure 7: Estimated SDB and corresponding relative vertical error for intertidal zone in Tauranga Harbour using waterline-derived (a1, b1, c1, and d1) and stumpf-ratio (a2, b2, c2, and d2) techniques. Background image: ESA Sentinel 2A.

The Stumpf-derived SDB (Fig. 7: (a2), (b2), (c2), and (d2)) allows the water depth to be assessed on a pixel by pixel basis, with a resolution of 10 m in the case of Sentinel Copernicus data; however the associated error (RMSE=25 cm) is higher than the waterline-derived SDB (RMSE=20 cm). In the Stumpf-derived SDB, the intertidal zone becomes flatter; the positive and negative errors are located in the upper and lower parts of the tidal flats, respectively, while in the middle regions a better

https://doi.org/10.5194/nhess-2021-387
Preprint. Discussion started: 17 March 2022


Natural Hazards and Earth System Sciences Discussions

approximation is estimated (whiter colour dots). Because of the shallow water column in the intertidal zones, the relationship between the log-ratio and depth cannot be properly assessed because of the insufficient variability in the data used to define the log-ratio/depth relationship, which leads to a low coefficient of determination (R2=0.09) between the green/blue band ratio and the LiDAR depth in the intertidal zone during the calibration of Stumpf-ratio technique. This assumption is confirmed by the higher correlation coefficient (R2=0.31) obtained when the same method is applied to the deepest parts of the estuary.

3.3 The statistical and dynamical corrections

The uncorrected waterline-derived SDB, the statistically (see Sect. 3.1) and the dynamically corrected waterline-derived SDB results for each image are shown in Fig. 8. The overall RMSE is equal to 20, 18 and 19 cm for the uncorrected SDB, statistical and dynamical corrections, respectively. For the uncorrected SDB, the strong relationship between tide level and error in the SDB is once more presented. For instance, in the images acquired during the high and mid-tide (Fig. 8, images 6–9) are associated with the highest error values, while smaller errors occur during low-tide (Fig. 8, images 1–5).

The statistical correction is effective where the primary SDB presents strong bias (e.g. Fig. 8, images 4 and 9). However, for the cases where the uncorrected SDB is a good approximation (Fig. 8, images 1–3), the statistical correction worsens the bathymetric estimates, by increasing the corresponding bias. The dynamical correction is more effective in the cases where the waterline is extracted from images collected at mid to high-tides (Fig. 8; images 4–9), improving the RMSE values by 5 cm on average. However, during low tides (Fig. 8, images 1–3), the estimates can worsen by 10.5 cm on average.

https://doi.org/10.5194/nhess-2021-387
Preprint. Discussion started: 17 March 2022

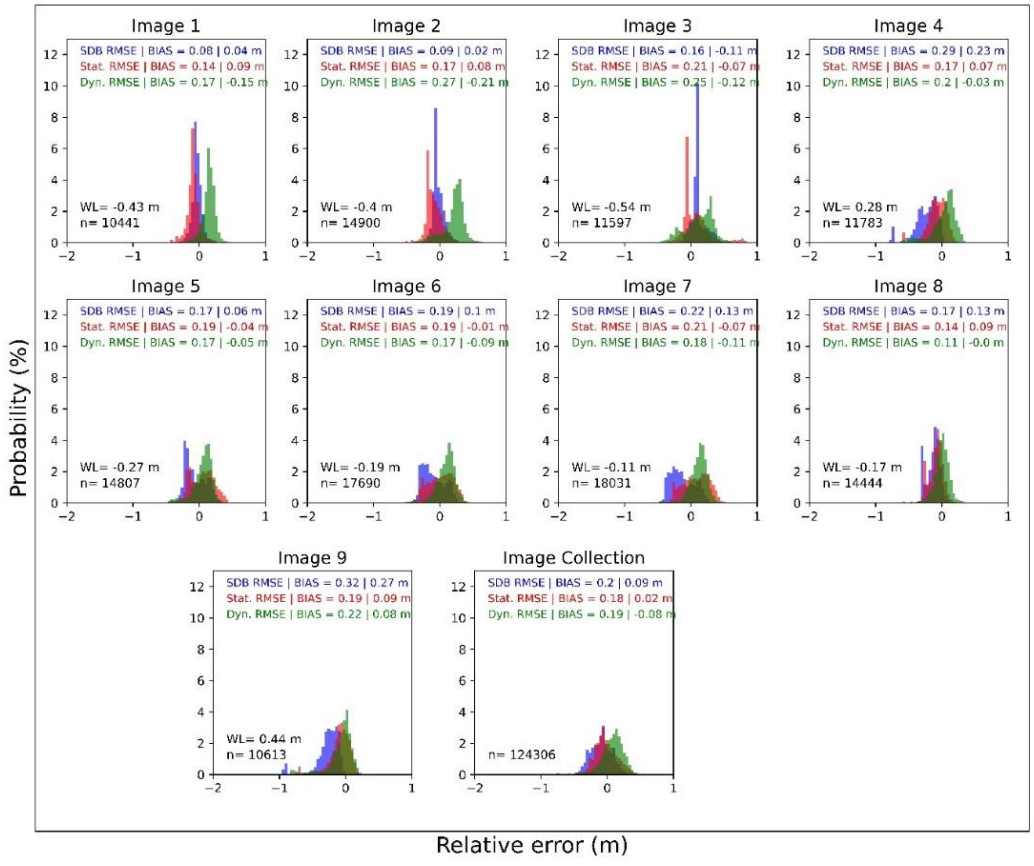

Figure 8: Histograms of the waterline-derived SDB relative error (RE) for each image in the collection for Tauranga Harbour: uncorrected SDB (blue), statistical correction (red) and dynamical correction (green). RMSE, BIAS, observed water level (WL), and number of waterline samples (n) are shown.

The limited improvement of the proposed corrections —2 and 1 cm in terms of RMSE, for statistical and dynamical corrections, respectively — can be due the limitations in the LiDAR data (survey performed in the year 2015, with +-20 cm vertical error), and hydrodynamic model predictions (average RMSE= 8cm and MAE = 20 cm), limiting the potential improvements that could be made to the method's accuracy.

In numerical models, although the waterline position is expected to be highly sensitive to the spatial grid resolution and interpolated bathymetry smoothness, the model is expected to obtain accurate water level predictions if properly calibrated and validated. To better illustrate the dynamical correction, we show the waterline position along three different profiles from Tauranga Harbour in Fig. 9. The uncorrected SDB is represented for these three different waterline positions (coloured circles: red, green, blue) with their corresponding heights (solid line) given from the observed water levels in the Ōmokoroa tide gauge at the time when the satellite acquires the image. The corresponding waterline position is also plotted with the height provided from the hydrodynamic model (triangles and dashed lines). The difference made by using the hydrodynamic model to assess the waterline height can vary spatially throughout the Harbour. For instance, while in P1 the dynamical correction generally

https://doi.org/10.5194/nhess-2021-387
Preprint. Discussion started: 17 March 2022

Natural Hazards and Earth System Sciences
Discussions

causes the height to be lower than the LiDAR height, whereas in P2, the SDB more closely represents the level measured by the LiDAR. In P3, the red and blue lines improve, whereas the green line worsens.

Some limitations in the waterline method can also be assessed by analysing the profiles in Fig. 9. For instance, in P2 and P3, the red and green observed waterlines are close to each other even though the tidal records show that the vertical difference should be almost 20 cm. However, when they are compared with the water level associated with the hydrodynamic model, they are roughly at the same elevation. The morphology in the intertidal area also plays a role. In P3, the terrain is quite steeply sloped, and in P2, the morphology undulates up and down which could cause some inaccuracies given that the resolution of the Sentinel-2 images is 10m. Additionally, it is important to note that regardless of whether there is a bimodal or unimodal distribution of the NDWI within in the intertidal zone, the Otsu threshold is defined by detecting the value that maximizes the within-class variance between two classes of a distribution. This means that even when all intertidal image pixels are flooded or dry, a threshold will be set and pixels will be selected as being the waterline, e.g. the peaks of high and low tide.

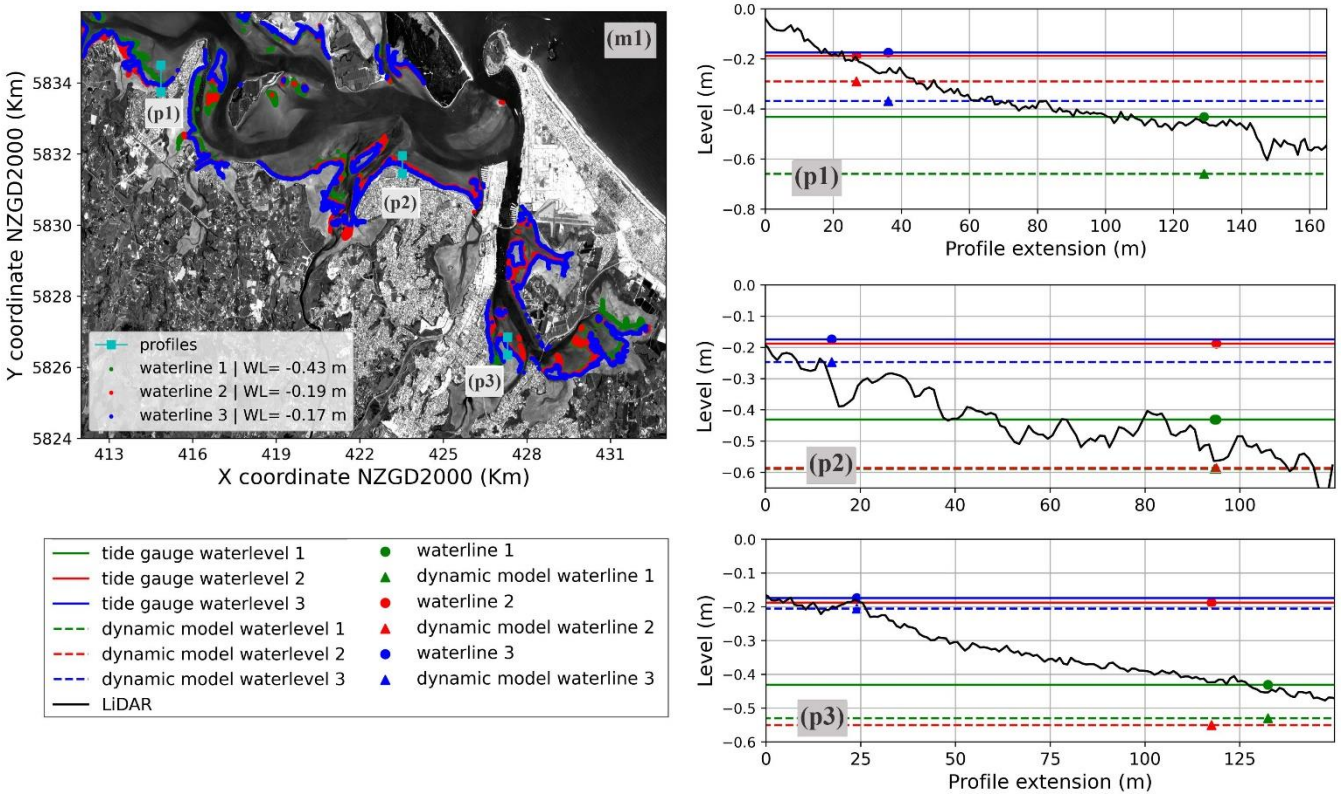

Figure 9: Profile analysis of the dynamical correction. [m1] Three waterline positions (blue, red, green) extracted from 3 different images corresponding to the observed water levels (WL) at Ōmokoroa. [p1, p2, p3] The position (dots) and WL (continuous lines) of the detected waterline and their corresponding dynamically corrected WL (dashed lines) and waterline position (triangles). The continuous black line is the LiDAR data along each profile. Background image: ESA Sentinel 2A.

https://doi.org/10.5194/nhess-2021-387
Preprint. Discussion started: 17 March 2022

Natural Hazards and Earth System Sciences Discussions

3.4 Prediction of water level using the SDB

The simulation scenarios showed that it is possible to obtain similar, or even enhanced water level predictions, by using the SDB rather than the surveyed bathymetry, Fig. 10. The average error parameters evaluated for observations from the three tide gauges (Ōmokoroa, Hairini and Oruamatua) show that, despite the lower density of estimated points, the use of waterline-derived SDB (S2) has a superior performance (RMSE=7.4 cm, MAE=24.3 cm, R2=0.97) to the Stumpf-derived SDB-S3 (RMSE=9.7 cm, MAE=29 cm, R2=0.96). The S4 scenario shows that by combining different SDB sources — waterline method for intertidal zones and Stumpf-ratio method for deeper areas of the estuary — it is possible to predict the astronomical tide with similar accuracy to using survey bathymetry (S1). Specifically at the location of the Oruamatua tide gauge, the predictions were strongly enhanced in the S4 scenario (RMSE=5cm; MAE=17cm) in comparison to S1 (RMSE=13cm; MAE=42cm), which can be seen in Fig. S8, Supplement D.

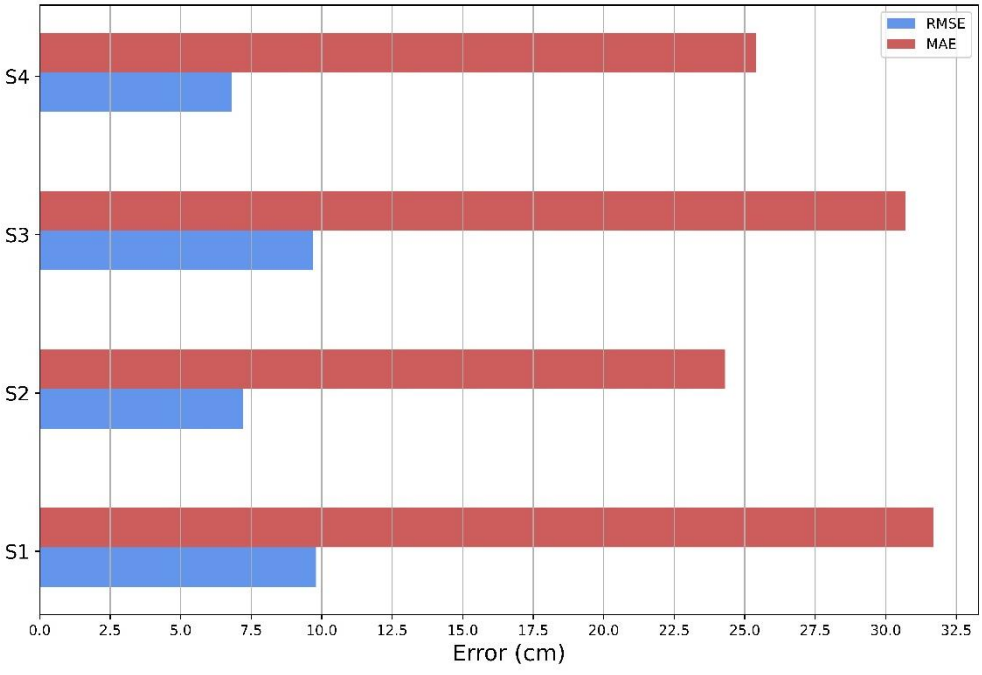

Figure 10: The average parameter errors of the four simulation scenarios (S1, S2, S3, and S4) — RMSE (blue bar), MAE (red bar) — for evaluated at the 3 tide gauge locations (Ōmokoroa, Hairini, Oruamatua).

The estuary's inner channels are where the major differences in the water level predictions occur, which reflects the numerical grid spatial resolution (20m) limitations in representing the flooding and drying within grid cells around narrow channels, as illustrated for the scenarios S1 and S4 in Fig. 11, referring to the differences in the maximum (panel (a)) and minimum (panel (b)) water level in each grid cell over the entire simulation. The occurrence of additional dry cells (e.g. in the harbour's northern and central region) is apparent in S4 when compared to S1 for highest (panel (a)) and lowest (panel (b)) water levels. This is

https://doi.org/10.5194/nhess-2021-387
Preprint. Discussion started: 17 March 2022

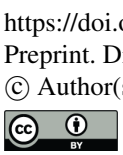

Natural Hazards and Earth System Sciences
Discussions

caused by the reflectance of areas covered by seagrass, that which interfere with the ability to detect the waterline/seabed using remote sensing.

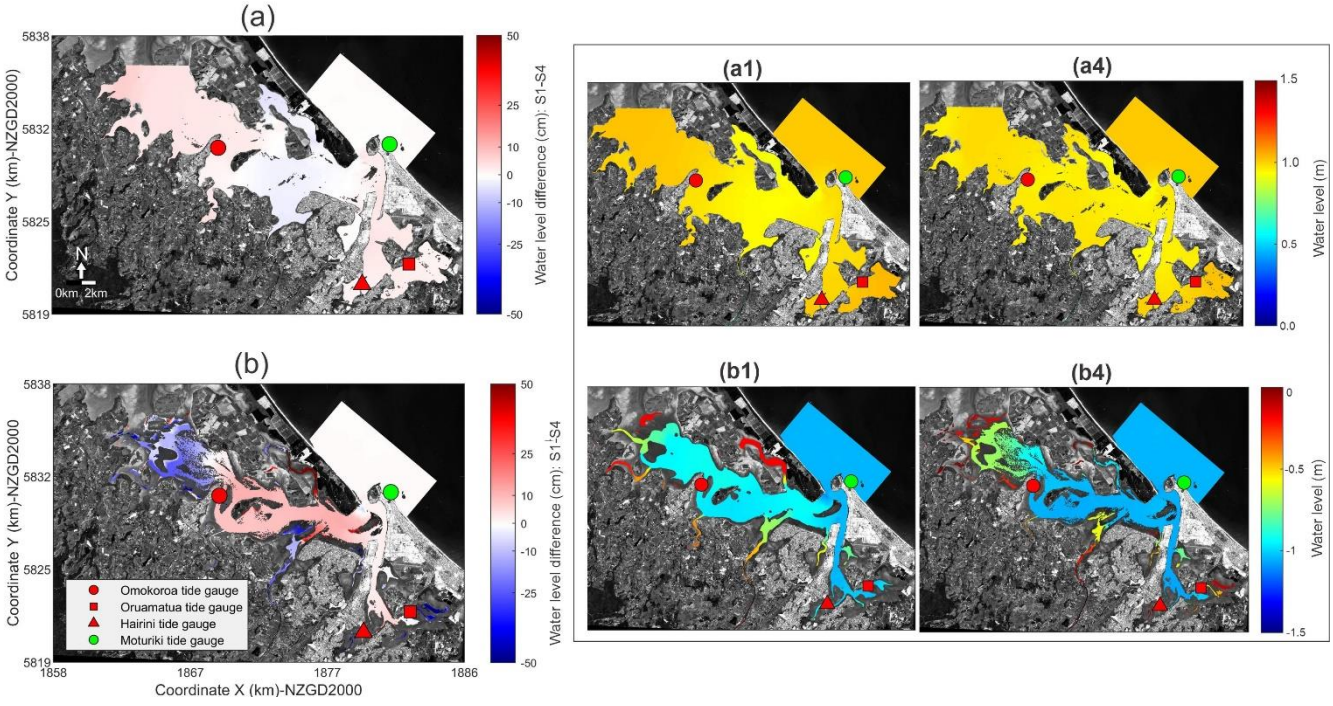

Figure 11: Spatial difference between the hydrodynamic model output using survey bathymetry (a1 and b1) and the waterline-derived plus Stumpf-ratio derived SDB (a4 and b4). High (a) and low tide condition (b), where positive means that the water level in S1 is higher than in S4. Background image: ESA Sentinel 2A.

4. Discussion

4.1 Insights about the waterline-method for satellite derived bathymetry

In our study, we used a waterline method to derive bathymetry from satellite images which has been trialled in other studies (Khan et al., 2019; Mason and Davenport, 1996; Ryu et al., 2002). Although our proposed correction methods (i.e. statistical and dynamical) for the SDB only resulted in 1–2 cm improvement across the estuary, our insights into why and where the correction resulted in improvements provide the basis for further work (e.g. when more imagery becomes available to test error sources more thoroughly). The statistical relationship between the error and the observed local water level, the elevation on the tidal flat and the waterline detection threshold in all 4 studied estuaries allowed us to set a semi-independent framework to correct the vertical level in the waterline-derived SDB. For instance, we can learn the relation between THLD and MRE in similar estuaries, and then apply the correction to an entirely different study area that has similar environmental properties (e.g. intertidal zone sediment colour, water turbidity/colour, spring tidal range and the coverage of the intertidal area relative to the overall area of the estuary). At this stage, the dynamical correction did not significantly improve the SDB because of the

https://doi.org/10.5194/nhess-2021-387
Preprint. Discussion started: 17 March 2022


Natural Hazards and Earth System Sciences Discussions

limitations in model performance and LiDAR data; however, similar approaches have been tested and validated for open estuarine areas proving that the effects of tidal propagation can be corrected (Bishop-Taylor et al., 2019; Khan et al., 2019; Mason et al., 1997).

Regarding the error source in the waterline method, our findings are similar to previous studies in that errors originated from the estuary's complex morphology, tidal range covered by the satellite images, and the ratio between water level and flooding/drying area in the tidal flat (Bué et al., 2020; Liu et al., 2013; Mason et al., 2001). In addition, the environmental conditions and unexpected variations in the image reflectance caused by seagrass banks (Ha et al., 2020) and/or groundwater seepage (Huisman et al., 2011), could also affect the SDB accuracy, likely contributing to our waterline-SDB being shallower than the LiDAR over the lower intertidal.

In comparison to other SDB techniques, our method showed a better or similar performance. For instance, the waterline method is an improvement on the Stumpf-ratio method (Caballero and Stumpf, 2019; Stumpf et al., 2003), despite the higher density of estimated water depth points (pixel-by-pixel resolution) that this log-ratio method offers. In addition, our method does not depend on calibration with surveyed bathymetry in order to establish a vertical reference (Jupp, 1989; Lyzenga, 1985; Stumpf et al., 2003). However, more accurate bathymetric derivations could be generated if physical based algorithms such SOA (Lee et al., 2011; Wei et al., 2020) or water turbidity correction methods (Caballero and Stumpf, 2020) were applied. In comparison to previous work using the SAR waterline techniques in larger and open estuaries and coastal areas (Bell et al., 2016; Catalao and Nico, 2017; Mason and Davenport, 1996), similar methods using waterline method and optical images (Bishop-Taylor et al., 2019; Khan et al., 2019; Sagar et al., 2017), and logistic regression approach (Bué et al., 2020), our approach can lead to average errors in the same order of magnitude (14 to 40 cm).

The use of an adaptive waterline threshold based on the Otsu method (Nobuyuki Otsu, 1979) showed good performance for determining the waterline location in estuaries, corroborating results of similar studies on lakes, rivers, water reservoirs (Donchyts et al., 2016), and coastlines (Vos et al., 2019). For our study site, this approach performed better if compared to the thresholds determined by the mean, or the median of NDWI distribution as used in previous studies (Bishop-Taylor et al., 2019; Sagar et al., 2017)

4.2 Hydrodynamic modelling assessment

Bathymetric data are fundamental for solving the hydrodynamic equations in shallow water; hydrodynamic models and flooding risk assessments in coasts and estuaries are therefore highly sensitive to depth values (Cea and French, 2012; Parodi et al., 2020; Pedrozo-Acuña et al., 2012). Our results show that inaccuracies occur especially in inner channels and seagrass banks, which means that the prediction of local short-term water level responses could be significantly affected. However, during the high tide, the resulting water level from SDB and survey scenarios are in good agreement in the majority of the simulated estuary domain and at the location of the tide gauges. Additionally, the overall shape of the bathymetry together with the length of estuary are the factors that affect the tidal response to sea-level rise in these environments (Du et al., 2018),

https://doi.org/10.5194/nhess-2021-387
Preprint. Discussion started: 17 March 2022


Natural Hazards and Earth System Sciences Discussions

which lead us to conclude that minor/ local irregularities in the bathymetry estimates do not substantially affect long term predictions for coastal management application.

Although the differences in the resulting water level between the SDB and in-situ bathymetry simulation scenarios compare well, our simulations were only conducted in one estuary (albeit a large and relatively complex estuary). Numerical simulations considering other estuaries and the storm surge should be evaluated as well, in order to know whether the errors on the SDB estimation could affect the tide-surge interactions, which is an important process to be considered in water level modelling (Spicer et al., 2019; Wankang et al., 2019; Zheng et al., 2020).

5. Conclusions

A waterline technique for deriving bathymetry from multispectral satellite images was developed and its use in hydrodynamic modelling assessed. The simple pre-processing required for the satellite images combined with the use of cloud computing and storage make the present framework highly applicable to regional scale studies. Our main findings show that the accuracy of the waterline SDB is similar or even superior to other techniques applied in previous studies. The accuracy of the LiDAR measurements and hydrodynamic model limit the efficacy of the statistical and dynamical corrections. Our major findings in the hydrodynamic modelling assessment showed that SDB techniques have an encouraging potential for use in water level predictions, considering the scenarios using different applications of the SDB did not show major differences over most of the domain. Moreover the use of SDB for hydrodynamic modelling in estuaries can make flooding assessment for remote coastal areas feasible, and provide a pathway around the need for expensive surveys for economically depressed vulnerable areas.

Code availability

The codes used in this work are available as python notebooks in https://github.com/CostaAndCoasts/Intertidal-zones-satellite-derived-bathymetry.

Credit authorship contribution statement

Wagner L.L. Costa: methodology, data analysis, writing – original draft, visualization. Karin R. Bryan: conceptualization, supervision, writing – review & editing, resources, funding acquisition. Giovanni Coco: Writing – review & editing, supervision.

https://doi.org/10.5194/nhess-2021-387
Preprint. Discussion started: 17 March 2022

Acknowledgment

The authors would like to thank Dr. Ben Stewart for numerical modelling assistance. This work was supported by the National Science Challenge: Resilience Challenge "Coasts" programme, GNS-RNC040. Data were supplied by Land Information New Zealand (LINZ), Bay of Plenty Regional Council, and Waikato Regional Council.

References

Bell, P. S., Bird, C. O. and Plater, A. J.: A temporal waterline approach to mapping intertidal areas using X-band marine radar, Coast. Eng., 107, 84–101, doi:10.1016/j.coastaleng.2015.09.009, 2016.

Bishop-Taylor, R., Sagar, S., Lymburner, L. and Beaman, R. J.: Between the tides: Modelling the elevation of Australia's exposed intertidal zone at continental scale, Estuar. Coast. Shelf Sci., 223(October 2018), 115–128, doi:10.1016/j.ecss.2019.03.006, 2019.

Bué, I., Catalão, J. and Semedo, Á.: Intertidal Bathymetry Extraction with Multispectral Images: A Logistic Regression Approach, Remote Sens., 12(8), 1311, doi:10.3390/rs12081311, 2020.

Caballero, I. and Stumpf, R. P.: Retrieval of nearshore bathymetry from Sentinel-2A and 2B satellites in South Florida coastal waters, Estuar. Coast. Shelf Sci., 226(June), 106277, doi:10.1016/j.ecss.2019.106277, 2019.

Caballero, I. and Stumpf, R. P.: Towards routine mapping of shallow bathymetry in environments with variable turbidity: Contribution of sentinel-2A/B satellites mission, Remote Sens., 12(3), doi:10.3390/rs12030451, 2020.

Catalao, J. and Nico, G.: Multitemporal Backscattering Logistic Analysis for Intertidal Bathymetry, IEEE Trans. Geosci. Remote Sens., 55(2), 1066–1073, doi:10.1109/TGRS.2016.2619067, 2017.

Cea, L. and French, J. R.: Bathymetric error estimation for the calibration and validation of estuarine hydrodynamic models, Estuar. Coast. Shelf Sci., 100, 124–132, doi:10.1016/j.ecss.2012.01.004, 2012.

Codiga, D. L.: Unified Tidal Analysis and Prediction Using the UTide Matlab Functions, , (September), 59, doi:10.13140/RG.2.1.3761.2008, 2011.

Donchyts, G., Schellekens, J., Winsemius, H., Eisemann, E. and van de Giesen, N.: A 30 m resolution surfacewater mask including estimation of positional and thematic differences using landsat 8, SRTM and OPenStreetMap: A case study in the Murray-Darling basin, Australia, Remote Sens., 8(5), doi:10.3390/rs8050386, 2016.

Du, J., Shen, J., Zhang, Y. J., Ye, F., Liu, Z., Wang, Z., Wang, Y. P., Yu, X., Sisson, M. and Wang, H. V.: Tidal Response to Sea-Level Rise in Different Types of Estuaries: The Importance of Length, Bathymetry, and Geometry, Geophys. Res. Lett., 45(1), 227–235, doi:10.1002/2017GL075963, 2018.

Ehses, J. S. and Rooney, J. J.: Depth Derivation Using Multispectral WorldView-2 Satellite Imagery, NOAA Tech. Memo. NMFS-PIFSC-46, (June), 24, doi:10.7289/V5668B40, 2015.

Emanuel, K.: Increasing destructiveness of tropical cyclones over the past 30 years, Nature, 436(7051), 686–688, doi:10.1038/nature03906, 2005.

https://doi.org/10.5194/nhess-2021-387
Preprint. Discussion started: 17 March 2022

Gao, J.: Bathymetric mapping by means of remote sensing: Methods, accuracy and limitations, Prog. Phys. Geogr., 33(1), 103–116, doi:10.1177/0309133309105657, 2009.

Gorelick, N., Hancher, M., Dixon, M., Ilyushchenko, S., Thau, D. and Moore, R.: Google Earth Engine: Planetary-scale geospatial analysis for everyone, Remote Sens. Environ., 202, 18–27, doi:10.1016/j.rse.2017.06.031, 2017.

Ha, N. T., Manley-Harris, M., Pham, T. D. and Hawes, I.: A Comparative Assessment of Ensemble-Based Machine Learning and Maximum Likelihood Methods for Mapping Seagrass Using Sentinel-2 Imagery in Tauranga Harbor, New Zealand, Remote Sens., 12(3), 355, doi:10.3390/rs12030355, 2020.

Huang, W. G., Fu, B., Zhou, C. B., Yang, J. S., Shi, A. Q. and Li, D. L.: Shallow water bathymetric surveys by spaceborne synthetic aperture radar, Int. Geosci. Remote Sens. Symp., 6(C), 2810–2812, doi:10.1109/igarss.2001.978171, 2001.

Huisman, C. E., Bryan, K. R., Coco, G. and Ruessink, B. G.: The use of video imagery to analyse groundwater and shoreline dynamics on a dissipative beach, Cont. Shelf Res., 31(16), 1728–1738, doi:10.1016/J.CSR.2011.07.013, 2011.

Hume, T., Gerbeaux, P., Hart, D., Kettles, H. and Neale, D.: A classification of New Zealand's coastal hydrosystems, , (October), 120, 2016.

Jawak, S. D., Vadlamani, S. S. and Luis, A. J.: A Synoptic Review on Deriving Bathymetry Information Using Remote Sensing Technologies: Models, Methods and Comparisons, Adv. Remote Sens., 4(2), 147–162, doi:10.4236/ars.2015.42013, 2015.

Jupp, D. L. B.: Background and extensions to depth of penetration (DOP) mapping in shallow coastal waters, Collect. Conf. Pap. Descr. Remote Sens. Appl. Proj. using microBRIAN image Process. Syst., 1989.

Khan, M. J. U., Ansary, M. N., Durand, F., Testut, L., Ishaque, M., Calmant, S., Krien, Y., Saifu, A. K. M. and Papa, F.: High-resolution intertidal topography from sentinel-2 multi-spectral imagery: Synergy between remote sensing and numerical modeling, Remote Sens., 11(24), 1–20, doi:10.3390/rs11242888, 2019.

Lee, Z., Franz, B., Shang, S., Dong, Q. and Arnone, R.: Some insights of spectral optimization in ocean color inversion, Remote Sens. Ocean. Sea Ice, Coast. Waters, Large Water Reg. 2011, 8175, 817508, doi:10.1117/12.897875, 2011.

Liu, Y., Li, M., Zhou, M., Yang, K. and Mao, L.: Quantitative analysis of the waterline method for topographical mapping of tidal flats: A case study in the dongsha sandbank, china, Remote Sens., 5(11), 6138–6158, doi:10.3390/rs5116138, 2013.

Lorensen, W. E. and Cline, H. E.: Marching cubes: A high resolution 3D surface construction algorithm, Proc. 14th Annu. Conf. Comput. Graph. Interact. Tech. SIGGRAPH 1987, 21(4), 163–169, doi:10.1145/37401.37422, 1987.

Lyzenga, D. R.: Shallow-water bathymetry using combined lidar and passive multispectral scanner data, Int. J. Remote Sens., 6(1), 115–125, doi:10.1080/01431168508948428, 1985.

Lyzenga, D. R., Malinas, N. P. and Tanis, F. J.: Multispectral bathymetry using a simple physically based algorithm, IEEE Trans. Geosci. Remote Sens., 44(8), 2251–2259, doi:10.1109/TGRS.2006.872909, 2006.

Mason, D., Hill, D., Davenport, I., Flather, R. and Robinson, G.: Improving inter-tidal digital elevation models constructed by the waterline technique, Eur. Sp. Agency, (Special Publ. ESA SP, (414 PART 2), 1079–1082, 1997.

Mason, D. C. and Davenport, L. J.: Accurate and efficient determination of the shoreline in ERS-1 SAR images, IEEE Trans. Geosci. Remote Sens., 34(5), 1243–1253, doi:10.1109/36.536540, 1996.

480 Mason, D. C., Davenport, I. J., Flather, R. A., Gurney, C., Robinson, G. J. and Smith, J. A.: A sensitivity analysis of the waterline method of constructing a digital elevation model for intertidal areas in ERS SAR scene of Eastern England, Estuar. Coast. Shelf Sci., 53(6), 759–778, doi:10.1006/ecss.2000.0789, 2001.

Mason, D. C., Scott, T. R. and Dance, S. L.: Remote sensing of intertidal morphological change in Morecambe Bay, U.K., between 1991 and 2007, Estuar. Coast. Shelf Sci., 87(3), 487–496, doi:10.1016/j.ecss.2010.01.015, 2010.

485 McFeeters, S. K.: The use of the Normalized Difference Water Index (NDWI) in the delineation of open water features, Int. J. Remote Sens., 17(7), 1425–1432, doi:10.1080/01431169608948714, 1996.

Morris, A. B. D., Coco, G., Bryan, K. R., Turner, I. L., Morris, B. D., Coco, G., Bryan, K. R., Turner, I. L., Street, K. and Vale, M.: Video-derived mapping of estuarine evolution Stable URL : https://www.jstor.org/stable/26481623 Linked references are available on JSTOR for this article : Video-derived mapping of estuarine evolution, , (50), 410–414, 2021.

490 Murray, N. J., Phinn, S. R., DeWitt, M., Ferrari, R., Johnston, R., Lyons, M. B., Clinton, N., Thau, D. and Fuller, R. A.: The global distribution and trajectory of tidal flats, Nature, 565(7738), 222–225, doi:10.1038/s41586-018-0805-8, 2019.

Nicholls, R. J. and Cazenave, A.: Sea-level rise and its impact on coastal zones, Science (80-.)., 328(5985), 1517–1520, doi:10.1126/science.1185782, 2010.

Nobuyuki Otsu: A Threshold Selection Method from Gray-Level Histograms, IEEE Trans. Syst. Man Cybern, 9(1), 62–66,

495 1979.

Oppenheimer, M., Glavovic, B., Hinkel, J., van de Wal, R., Magnan, A. K., Abd-Elgawad, A., Cai, R., Cifuentes-Jara, M., DeConto, R. M., Ghosh, T., Hay, J., Isla, F., Marzeion, B., Meyssignac, B. and Sebesvari, Z.: Sea Level Rise and Implications for Low Lying Islands, Coasts and Communities., IPCC Spec. Rep. Ocean Cryosph. a Chang. Clim., 355(6321), 126–129, doi:10.1126/science.aam6284, 2019.

500 Parodi, M. U., Giardino, A., Van Dongeren, A., Pearson, S. G., Bricker, J. D. and Reniers, A. J. H. M.: Uncertainties in coastal flood risk assessments in small island developing states, Nat. Hazards Earth Syst. Sci., 20(9), 2397–2414, doi:10.5194/nhess-20-2397-2020, 2020.

Pedrozo-Acuña, A., Ruiz de Alegria-Arzaburu, A., Mariño-Tapia, I., Enriquez, C. and González Villareal, F. J.: Factors controlling flooding at the Tonalá river mouth (Mexico), J. Flood Risk Manag., 5(3), 226–244, doi:10.1111/j.1753-

505 318X.2012.01142.x, 2012.

Ryu, J. H., Won, J. S. and Min, K. D.: Waterline extraction from Landsat TM data in a tidal flat a case study in Gomso Bay, Korea, Remote Sens. Environ., 83(3), 442–456, doi:10.1016/S0034-4257(02)00059-7, 2002.

Sagar, S., Roberts, D., Bala, B. and Lymburner, L.: Extracting the intertidal extent and topography of the Australian coastline from a 28 year time series of Landsat observations, Remote Sens. Environ., 195, 153–169, doi:10.1016/j.rse.2017.04.009,

510 2017.

Sobel, A. H., Camargo, S. J., Hall, T. M., Lee, C., Tippett, M. K. and Wing, A. a: Cyclone Intensity, Science (80-.)., 353(6296), 2016.

Spicer, P., Huguenard, K., Ross, L. and Rickard, L. N.: High-Frequency Tide-Surge-River Interaction in Estuaries: Causes and

https://doi.org/10.5194/nhess-2021-387
Preprint. Discussion started: 17 March 2022

Implications for Coastal Flooding, J. Geophys. Res. Ocean., 124(12), 9517–9530, doi:10.1029/2019JC015466, 2019.

Stumpf, R. P., Holderied, K. and Sinclair, M.: Determination of water depth with high-resolution satellite imagery over variable bottom types, Limnol. Oceanogr., 48(1), 547–556, 2003.

Vos, K., Splinter, K. D., Harley, M. D., Simmons, J. A. and Turner, I. L.: CoastSat: A Google Earth Engine-enabled Python toolkit to extract shorelines from publicly available satellite imagery, Environ. Model. Softw., 122, 104528, doi:10.1016/j.envsoft.2019.104528, 2019.

Van Der Walt, S., Schönberger, J. L., Nunez-Iglesias, J., Boulogne, F., Warner, J. D., Yager, N., Gouillart, E. and Yu, T.: Scikit-image: Image processing in python, PeerJ, 2014(1), 1–18, doi:10.7717/peerj.453, 2014.

Wankang, Y., Baoshu, Y., Xingru, F., Dezhou, Y., Guandong, G. and Haiying, C.: The effect of nonlinear factors on tide-surge interaction: A case study of Typhoon Rammasun in Tieshan Bay, China, Estuar. Coast. Shelf Sci., 219(January), 420–428, doi:10.1016/j.ecss.2019.01.024, 2019.

Webster, P. J., Holland, G. J., Curry, J. A. and Chang, H. R.: Atmospheric science: Changes in tropical cyclone number, duration, and intensity in a warming environment, Science (80-.)., 309(5742), 1844–1846, doi:10.1126/science.1116448, 2005.

Wei, J., Wang, M., Lee, Z., Briceño, H. O., Yu, X., Jiang, L., Garcia, R., Wang, J. and Luis, K.: Shallow water bathymetry with multi-spectral satellite ocean color sensors: Leveraging temporal variation in image data, Remote Sens. Environ., 250(April), 112035, doi:10.1016/j.rse.2020.112035, 2020.

Zheng, P., Li, M., Wang, C., Wolf, J., Chen, X., De Dominicis, M., Yao, P. and Hu, Z.: Tide-Surge Interaction in the Pearl River Estuary: A Case Study of Typhoon Hato, Front. Mar. Sci., 7(April), 1–21, doi:10.3389/fmars.2020.00236, 2020.